On the resolution of density anomalies in the Earth's mantle using spectral fitting of normal-mode data

Chaincy Kuo* and Barbara Romanowicz

Department of Earth and Planetary Sciences and Seismological Laboratory, University of California, Berkeley, CA, USA. E-mail: chaincy@cal.berkeley.ed

SUMMARY

The resolution of the 3-D density structure in the Earth's deep interior has long eluded geoscientists. High-quality data from digital seismic instruments emplaced this decade have renewed interest in the measurement of low-frequency Earth normal modes with the goal of extracting heterogeneous density structure. Here we perform a series of synthetic experiments aimed at investigating the resolution of lateral variations in the mantle from normal-mode spectral data. Contamination effects between seismic velocities and density are examined in two ways: (1) by using resolution matrices computed from data kernels and (2) by inverting synthetic spectra computed from realistic input Earth models. The first type of experiment assumes that the non-linearity of the inverse problem is weak. No such assumptions are necessary in the second type of tests which, nevertheless concur in their results with the former. These synthetic tests indicate that density structure retrieved from presently available normal-mode data is not reliable. Contamination of seismic velocity structure into the density model space produces patterns that resemble those obtained from inversions of real data. The resulting density models appear to be dependent on a combination of the starting velocity models and the model parametrization.

Key words: density, mantle, normal modes, seismic tomography.

INTRODUCTION

The issue of whether lateral variations in density in the mantle can be resolved from normal-mode data has recently received renewed attention, in particular with the work of Ishii & Tromp (1998, 1999). These authors present a degree-six model of density throughout the mantle, derived from inversion of normal-mode splitting coefficients. This model presents unexpected features in the lowermost mantle, namely two large 'blobs' of high-density material centred in the Pacific and under Africa, that, if real, could have important consequences for the dynamics of the mantle. Ishii & Tromp (1999) argue for the robustness of their model, on the basis of numerous experiments, including checkerboard resolution tests and exploration of different parametrization schemes.

Whether lateral variations in density can be resolved from normal-mode data has long been the subject of debate. Resovsky & Ritzwoller (1999a) have recently presented the results of tests that show that the retrieved density structure is very sensitive to the regularization scheme used in the inversion. Imposed *a priori* constraints on the location and size of density heterogeneity have a strong effect on the resulting models, which, while providing an equally good fit to the data, can be significantly different. Ishii & Tromp (1999),

however, argue that their density model is weakly dependent on their starting model. More recently, Romanowicz (2001) performed a series of experiments using a set of well-constrained degree-two splitting coefficients for mantle modes, similar to that of Ishii & Tromp (2001). In particular, she showed by forward modelling that, in the bottom 1000 km of the mantle, the sign of the correlation of density with velocity could not be resolved, even at degree two, at least with the presently available mode data set.

In what follows, we present the results of a series of tests in which we have explored more fully the structure of the resolution matrix than can be obtained with checkerboard tests (e.g. Lévêque *et al.* 1993). Because, in the case of non-linear inversions, the resolution matrix approach only allows us to investigate the problem approximately (e.g. Tarantola 1987), we also present results of tests in which we compute synthetic seismograms for realistic Earth models and invert them under the same conditions as the real data.

SYNTHETIC DATA

In the experiments presented here we use a synthetic data set and inversion scheme that mimics the actual data set and methodology that we have used in a study of 3-D mantle structure based on real mode data (Kuo & Romanowicz 1999a,b). This mode data set comprises the spectra of 44 spheroidal modes observed on the vertical component, including seven pairs of coupled modes that provide

*Now at: Xenogen Corporation, 860 Atlantic Ave, Alameda, CA 94501-2200, USA.

some sensitivity to odd-degree structure. The analysis method is a one-step inversion scheme in which mantle structure in $\delta \ln V_s$, $\delta \ln V_p$ and $\delta \ln \rho$ is derived directly from the observed spectra. This method is described fully in Kuo (1999) (including multiplet coupling) and the self-coupling part can be found in Durek & Romanowicz (1999). It was developed following the work of Li *et al.* (1991). This contrasts with the approach of some recent studies, which use a two-step procedure, involving the computation of splitting coefficients followed by an inversion for 3-D structure (e.g. Ishii & Tromp 1999; Resovsky & Ritzwoller 1999b). The advantage of the one-step inversion method is that we are solving directly for a model compatible with the spectra of all the modes in the data set. Incompatibilities in the data can thus be treated in a more robust fashion. In the two-step procedure, the first, non-linear step is performed separately for each mode, yielding 'splitting functions' (Woodhouse *et al.* 1986) that are not required to be all consistent with a single earth model. If some mode measurements are biased, they may thus weigh more heavily in the second step, linear inversion relating splitting functions to the 3-D elastic model of the mantle.

The advantage of including coupled modes such as $_1S_4-_2S_5$ and $_1S_5-_2S_6$ is that some components of odd-degree structure can then also be retrieved, in addition to even-degree structure. However, in the discussion that follows, we focus on the even-degree structure (and therefore the isolated multiplets), as this has been the framework of other studies, in particular, that of Ishii & Tromp (1999).

We synthesize very-long-period data from GSN/IRIS and Geoscope stations for the same eight events as were used with real data in an attempt to retrieve a 3-D density model of the mantle (Kuo 1999). The events are listed in Table 1. They were selected according to their size ($M_0 \geq 5 \times 10^{20}$ N m) and their occurrence preceding and following a relatively quiet period in seismicity, so that about 125 h of data could be obtained from each record, free of perturbations from major aftershocks or other earthquakes with $M_w \geq 6.5$ ($M_0 \geq 7 \times 10^{18}$ N m). Only vertical component records were considered (spheroidal modes only). Deep events ($h > 200$ km) were favoured, since they excite mode branches sensitive to very deep structure better than shallow earthquakes of the same size.

Synthetic time-domain traces were calculated using the 3-D *SH* velocity model SAW12D (Li & Romanowicz 1996), and source characteristics from the CMT catalogue (e.g. Dziewonski *et al.* 1995) were assumed in the forward modelling of the traces. In order to mimic the real data preparation process, the traces were deconvolved to ground acceleration, and a tapered bandpass filter was applied. The records were then Fourier transformed using a length of record determined in preparation of real data in which the signal-to-noise ratio and the isolation from neighbouring modes are optimized. When using a Hann window, the duration is typi-

cally targeted to be about 1.1Q-cycles of the mode (Dahlen 1982) to optimize the estimation of frequencies and decay rates of well-isolated modes. Some target multiplets are close in frequency to low-Q neighbours, and it is advantageous to initiate the Hann window a few hours after the origin time of the event in order to allow the neighbouring modes to decay and bring out the signal amplitude of the target mode. The traces are then padded with zeros before the application of a fast Fourier transform algorithm to the frequency domain. The frequency window limits are chosen for each mode, and do not vary between stations and events.

We use the vertical component spectra of spheroidal mantle modes, the eigenfunctions of which primarily exhibit particle motion in the mantle ($_0S, _1S, _2S, _4S, _5S$ branches, and a few in the $_6S, _7S, _8S$ branches). Modes with significant displacement in the core are not included in this study, although some mantle modes in our data set have some sensitivity to outer core structure. The effect of outer core sensitivity on our models of mantle structure is minimal, and this is consistent with the conclusions of Giardini *et al.* (1987). Below 5 mHz, the mantle modes in our study are well isolated in frequency, which minimizes contamination by neighbouring modes. On the other hand, our analysis code is capable of taking into account the more complex effects of 3-D structure on the spectra of coupled mode pairs. In total, we have chosen 30 isolated mantle modes and seven coupled mantle mode pairs, amounting to a total of 44 spheroidal mantle modes (Table 2), and spectra from a total of 2757 individual seismograms. From each spectrum, about ~10–20 data points are used.

TESTS WITH RESOLUTION MATRICES

Resolution matrix

The resolution matrix is a useful tool for assessing the leakage between model parameters in a generalized inversion framework, when the non-linearity of the problem is not too strong. Indeed, the solution $\mathbf{m}_{est}$ to the inverse problem $\mathbf{d}_{obs} = \mathbf{Am}$, where $\mathbf{A}$ is a linearized data kernel (Kuo 1999), $\mathbf{d}_{obs}$ is the data vector and $\mathbf{m}$ is the model vector, can be written as (e.g. Menke 1989)

$$\mathbf{m}_{est} = \left(\mathbf{A}^T\mathbf{A} + \mathbf{C}_m^{-1}\right)^{-1}\mathbf{A}^T\mathbf{d}_{obs}, \tag{1}$$

where $\mathbf{C}_m^{-1}$ is the model covariance matrix. The relation between the vector of estimated model parameters $\mathbf{m}_{est}$ and the true model $\mathbf{m}_{true}$, for a given parametrization and underlying theory, is then:

$$\mathbf{m}_{est} = \left(\mathbf{A}^T\mathbf{A} + \mathbf{C}_m^{-1}\right)^{-1}\mathbf{A}^T\mathbf{Am}_{true}. \tag{2}$$

The $M \times M$ model resolution matrix $\mathbf{R}$, where M is the number of unknown parameters, is defined as

$$\mathbf{R} = \left(\mathbf{A}^T\mathbf{A} + \mathbf{C}_m^{-1}\right)^{-1}\mathbf{A}^T\mathbf{A} \tag{3}$$

so that

$$\mathbf{m}_{est} = \mathbf{Rm}_{true}. \tag{4}$$

If $\mathbf{R} = \mathbf{I}$, where $\mathbf{I}$ is the identity matrix, then each model parameter is perfectly resolved. In practice, $\mathbf{R}$ has non-zero off-diagonal terms, and their size relative to each other and to the diagonal terms indicates the amount of contamination between the different parameters as determined by inversion.

In our particular problem, we invert simultaneously for structure in V_P, V_S and ρ, and wish to investigate the level of contamination between these parameters. The model vector is arranged as follows:

Table 1. Earthquake event information.

Date	Moment ($\times 10^{20}$ N m)	M_w	Depth (km)	Region
03/09/94	3.5	7.63	564	Fiji Islands
06/09/94	30.5	8.26	637	Northern Bolivia
10/04/94	33.9	8.29	33	Kurile Islands
07/30/95	13.8	8.03	47	Northern Chilean Coast
10/09/95	13.3	8.02	49	Coast Near Jalisco, Mexico
01/01/96	8.8	7.90	33	Minahassa Peninsula
02/17/96	27.5	8.23	33	West Irian Region
06/17/96	8.2	7.88	587	Flores Sea

Table 2. List of modes included in the kernel matrix. The central reference frequency of each mode, with respect to PREM, is listed in the second column.

Mode(s)	Reference frequency (mHz)
$_0S_3$	0.469
$_0S_4$	0.647
$_0S_5$	0.840
$_0S_6$	1.038
$_0S_9$	1.578
$_0S_{27}$	3.544
$_1S_2$	0.680
$_1S_4$	1.173
$_1S_7$	1.656
$_1S_8$	1.799
$_1S_9$	1.964
$_2S_6$	1.681
$_2S_{12}$	2.737
$_2S_{13}$	2.900
$_4S_2$	1.722
$_4S_4$	2.280
$_4S_9$	3.709
$_4S_{11}$	4.010
$_5S_3$	2.170
$_5S_4$	2.380
$_5S_5$	2.703
$_5S_6$	3.011
$_5S_7$	3.291
$_5S_8$	3.526
$_5S_{12}$	4.696
$_6S_{10}$	4.211
$_7S_4$	3.413
$_7S_5$	3.660
$_8S_7$	4.650
$_9S_{14}$	6.768
$_3S_1{-}_1S_3$	0.944, 0.940
$_2S_4{-}_2S_5$	1.379, 1.370
$_2S_5{-}_2S_6$	1.515, 1.522
$_4S_3{-}_2S_8$	2.049, 2.049
$_6S_3{-}_3S_8$	2.822, 2.820
$_0S_7{-}_2S_3$	1.232, 1.242
$_2S_{10}{-}_4S_5$	2.403, 2.411

$$\mathbf{m} = \left[\delta \ln {}_pV_{P_s}^{\,t},\ \delta \ln {}_pV_{S_s}^{\,t},\ \delta \ln {}_p\rho_s^{\,t}\right], \tag{5}$$

where the indices s, t and p refer to the parametrization of the model. In our studies, we have chosen spherical harmonics as basis functions in the horizontal direction and associated Legendre polynomials in the vertical direction, as commonly used in mantle tomography (e.g. Woodhouse & Dziewonski 1984; Li & Romanowicz 1996). The maximum degree ($s_{max} = 6$) of the spherical harmonics expansion is chosen in view of the sensitivity of the particular mode data set we are considering, given that a particular mode of angular order l is sensitive to at most lateral heterogeneity of degree $2l$. The maximum order of the radial polynomial expansion is commensurate with the maximum radial order n of the modes in our data set ($p_{max} = 7$). We conduct tests for $p_{max} = 7$ and 10. Ishii & Tromp (2001) radially overparametrize their models to order 13 using Chebyshev polynomials and damp higher-order polynomials more strongly.

The resolution equation is then:

$$\begin{bmatrix} \delta \ln {}_pV_{P_s}^{\,t} \\ \delta \ln {}_pV_{S_s}^{\,t} \\ \delta \ln {}_p\rho_s^{\,t} \end{bmatrix}_{est} = \begin{bmatrix} R_P & \emptyset_{SP} & \emptyset_{RP} \\ \emptyset_{PS} & R_S & \emptyset_{RS} \\ \emptyset_{PR} & \emptyset_{SR} & R_R \end{bmatrix} \begin{bmatrix} \delta \ln {}_pV_{P_s}^{\,t} \\ \delta \ln {}_pV_{S_s}^{\,t} \\ \delta \ln {}_p\rho_s^{\,t} \end{bmatrix}_{true} \tag{6}$$

where R_P, R_S and R_R are resolution submatrices for $\delta \ln {}_pV_{P_s}^{\,t}$, $\delta \ln {}_pV_{S_s}^{\,t}$ and $\delta \ln {}_p\rho_s^{\,t}$, respectively, and non-zero values in $\emptyset_{PS}$ indicate the correlations that would map V_P structure into V_S structure, and so on. The $\emptyset$s are zero in an ideal resolution matrix.

Imposing a priori distributions. Since the resolution matrix is a function of both the data kernels and the *a priori* model covariance matrix, C_m^{-1}, it is important to choose the *a priori* elements of C_m^{-1} carefully, denoted as 'damping parameters', so as to obtain, inasmuch as possible, $\mathbf{R} \approx \mathbf{I}$.

To do so, we consider a 'realistic' synthetic model, for which we choose the S velocity ($\delta \ln V_S$) to be that of model SAW12D (Li & Romanowicz 1996), and P velocity ($\delta \ln V_P$) to be that of P16B30 (Bolton 1996). A mock density model ($\delta \ln \rho$) is constructed so that the root-mean-square amplitudes are about 25 per cent of $\delta \ln V_S$, which is a common assumption in low-frequency seismology (e.g. Li *et al.* 1991) that is in agreement with laboratory measurements at shallow mantle pressure and temperatures (Karato 1993). The mock density perturbations are constructed by permuting and scaling (to 25 per cent) coefficients of the $\delta \ln V_s$ model SAW12D so that the actual patterns of heterogeneity are not correlated with SAW12D, and we call this model R25. As mentioned previously, we consider two different spatial parametrizations: (1) $s_{max} = 6$, $p_{max} = 7$ (experiment A) and (2) $s_{max} = 6$, $p_{max} = 10$ (experiment B). The resolution matrix is computed using the data kernels corresponding to our data set of 44 spheroidal mode spectra.

Damping parameters are defined separately for $\delta \ln V_P$, $\delta \ln V_S$ and $\delta \ln \rho$ and chosen in such a fashion as to best recover the rms amplitudes of the given true model for even degrees (two, four and six) after applying the resolution matrix. We only consider norm damping (η_1) (Li & Romanowicz 1996), which are the diagonal terms of the model covariance matrix (C_m^{-1}). As our damping parameter strengths are scaled by the mean of the kernel matrix product with its transpose, we find that values of $\eta_1^P = \eta_1^S = \eta_1^R = 1$ are adequate for both spatial parametrizations (Figs 1a and c). Note that this choice of damping parameters is very close to that used in our inversions with real data (Kuo 1999), which, in turn, were chosen so as to recover amplitudes of $\delta \ln V_S$ and $\delta \ln V_P$ commensurate with those obtained in independent studies based on higher-frequency data. The odd-degree structure amplitudes are slightly overestimated owing to the inadequate constraints from only two mode pairs ($_1S_4{-}_2S_5$ and $_1S_5{-}_2S_6$) for degrees one, three and five, and three mode pairs ($_4S_3{-}_2S_8$, $_6S_3{-}_3S_8$ and $_2S_{10}{-}_4S_5$) for degree five only. It is interesting to note that in the depth ranges in which the rms amplitudes in $\delta \ln V_P$ and $\delta \ln V_S$ are decreased, the amplitudes in $\delta \ln \rho$ are increased (400–1200 and 1600–2400 km depth), potentially indicating leakage from the former to the latter. In Figs 1(b) and (d), the correlations between $\mathbf{m}_{true}$ and $\mathbf{m}_{est}$ are plotted for spatial parametrizations $s_{max} = 6$, $p_{max} = 7$ and $s_{max} = 6$, $p_{max} = 10$, respectively. We recover perturbations in V_P and V_S well for the spatial parametrization $s_{max} = 6$, $p_{max} = 7$, (correlation coefficients of 75–99 per cent), and perturbations in ρ are recovered with ~60 per cent correlation. For the spatial parametrization $s_{max} = 6$, $p_{max} = 10$, we can still recover perturbations in V_P and V_S sufficiently, although in the depth range 400–670 km, the correlation drops to ~50 per cent. Perturbations in ρ at the top of the lower mantle are poorly recovered in this parametrization. Clearly, adding vertical smoothing is necessary to compensate for overparametrization in the vertical direction.

If the patterns of perturbation in our input model $\mathbf{m}_{true}$ are the same for V_s, V_p and ρ, then a resolution experiment on such an $\mathbf{m}_{true}$ is insufficient to assess the leakage of $\delta \ln V_S$ and $\delta \ln V_P$
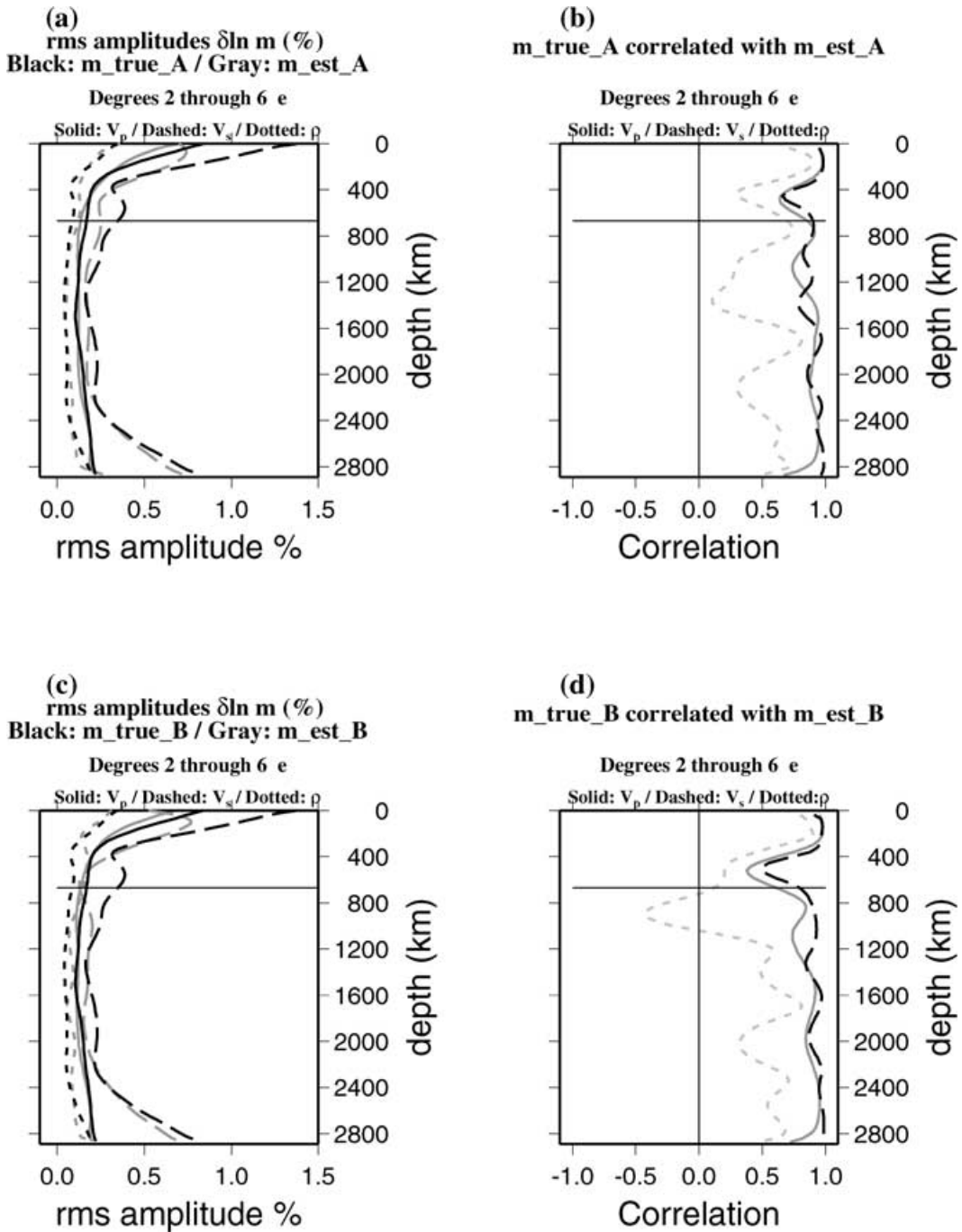
Figure 1. (a) For experiment A, the root-mean-squared amplitudes of an input model $\mathbf{m}_{\text{true}}$ in black lines, and output model $\mathbf{m}_{\text{est}}$ from a resolution matrix test, in grey lines. The dashed lines are $\delta \ln V_s$, the solid lines are $\delta \ln V_p$, and the dotted lines are $\delta \ln \rho$ rms amplitudes. See Table 1 for a description of input models. (b) The correlation of $\mathbf{m}_{\text{true}}$ with $\mathbf{m}_{\text{est}}$. The dashed line is the correlation of $\delta \ln V_s$ between the input and output models: solid line, $\delta \ln V_p$ and dotted line, $\delta \ln \rho$ (c) and (d) same as (a) and (b), respectively, for experiment B.

structure into $\delta \ln \rho$. However, it gives us an opportunity to examine the structure of the resolution matrix, which is independent of the input model coefficients. The resolution matrix is presented in Fig. 2, which shows that the part of the matrix corresponding to $\delta \ln V_S$ and $\delta \ln V_P$ has a structure close to that of an identity matrix, with the strongest values being on the diagonal, and generally weak cross-terms $\emptyset_{SP}$ and $\emptyset_{PS}$. On the other hand, the density submatrix shows both much smaller values on the diagonal, compared with $\delta \ln V_S$ and $\delta \ln V_P$, and off-diagonal terms $\emptyset_{RP}, \emptyset_{RS}, \ldots$, which are small but commensurate with the diagonal terms. The structure of

the resolution matrix indicates that density cannot be resolved as well as velocity structure. The relative level of damping between velocities and density will only act to scale the off-diagonal terms with the diagonal terms, and therefore contamination will always be present.

Many authors perform checkerboard tests to assess the resolution of their models. In this kind of test, the model vector $\mathbf{m}_{\text{true}}$ is sparsely populated by non-zero coefficients $_p m_s^t$. For example, a checkerboard model defined by $s = 4, t = 4$ and $p_{\max} = 7$ will consist of non-zero values for $_p m_4^4$ and $_p m_4^{-4}$ for $0 \le p \le 7$. This gives 16 non-zero
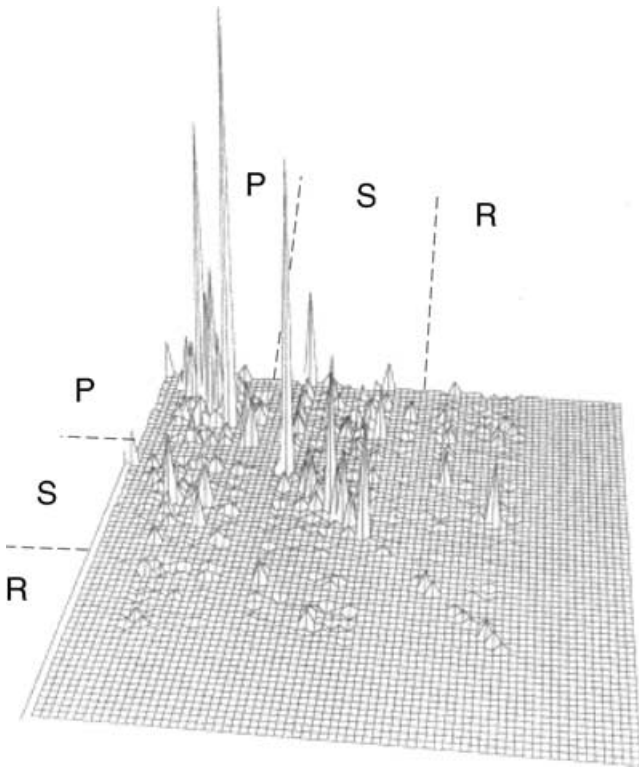
Figure 2. The resolution matrix for 44 spheroidal modes used in this study. The order of the model parameters is such that azimuthal orders are grouped with each harmonic degree, which increases down the diagonal, grouped by radial order, which increases down the diagonal. In order to visualize the full matrix, a spatial filter was applied to the pixel elements of the image. Therefore, each element does not necessarily correspond to a spectral coefficient.

elements in $\mathbf{m}_{\mathrm{true}}$, of dimension $M = 200$ ($M = (s+1)^2(p_{\max}+1)$, where the lateral degree-zero term is included). The remaining 184 elements of $\mathbf{m}_{\mathrm{true}}$ are zero. Then, many non-zero off-diagonal elements in $\mathbf{R}$ can be neutralized by the product with zero or very small valued elements in $\mathbf{m}_{\mathrm{true}}$, and the correlations in $\mathbf{R}$ may not be found by this type of test, even if it is performed at several degrees s (e.g. Lévêque *et al.* 1993).

Also, one may introduce a checkerboard model for $\delta \ln V_P$ only, where $\delta \ln V_S = 0$ and $\delta \ln \rho = 0$ in $\mathbf{m}_{\mathrm{true}}$, to analyse the possible mapping of V_P structure into V_S and ρ structure, or introduce a checkerboard pattern for $\delta \ln V_S$ only to analyse the possible mapping of V_S structure into V_P and ρ structure, and so on (Ishii & Tromp 1999, 2001). Then, for a checkerboard pattern $s = 4$, $t = 4$ and $p_{\max} = 7$ in only one physical parameter vector, there are 16 non-zero values populating $\mathbf{m}_{\mathrm{true}}$ of dimension $M = 600$ ($M = (s+1)^2(p_{\max}+1) \times 3$). Off-diagonal elements in $\mathbf{R}$ can be missed, unless checkerboard tests are run for each model coefficient, which is not generally done. Even so, if all coefficients are explored, small amounts of contamination into other model parameters may be observed for each coefficient and may be deemed negligible. In this case, the cumulative contamination of all coefficients from one model parameter into a particular coefficient of another model parameter is not assessed, nor is the pattern of the cumulative contamination. In other words, the mapping between physical parameters is not fully explored. This issue has been clearly illustrated by Lévêque *et al.* (1993).

Instead of using a checkerboard model, in a first set of experiments, we choose to fully populate δV_P (respectively, δV_S and $\delta \rho$)

with coefficients of an aspherical model, keeping the other parameters zero. We can thus test how well we can resolve each parameter, independently of the others, and how much is mapped into the others (e.g. Resovsky & Ritzwoller 1999b). Our input models are therefore, respectively, $\mathbf{m}_{\mathrm{true}}^P = [\delta \ln V_P, \emptyset, \emptyset]$ $\mathbf{m}_{\mathrm{true}}^S = [\emptyset, \delta \ln V_S, \emptyset]$ and $\mathbf{m}_{\mathrm{true}}^R = [\emptyset, \emptyset, \delta \ln \rho]$. The same model of heterogeneity is used in all three cases, but the amplitudes are scaled according to $\delta \ln V_P = 0.5\delta \ln V_S$ and $\delta \ln \rho = 0.25\delta \ln V_S$, to achieve realistic rms levels in the respective parameters being tested. Resolution experiments with parametrizations A and B, as defined above, are performed in each case.

In Figs 3–5, we plot the results of the three resolution tests using $\mathbf{m}_{\mathrm{true}}^P$, $\mathbf{m}_{\mathrm{true}}^S$ and $\mathbf{m}_{\mathrm{true}}^R$, respectively, for $s_{\max} = 6$, $p_{\max} = 7$. The legend scale for heterogeneity for $\delta \ln V_P$ is ± 1 per cent, for $\delta \ln V_S$ is ± 1.7 per cent, and for $\delta \ln \rho$ is ± 0.5 per cent. The colour scale is chosen so as to correspond to expected amplitudes for each physical parameter. Fig. 3 shows that $\delta \ln V_P$ is well recovered, but there is some contamination into $\delta \ln V_{S\,\mathrm{est}}$ and $\delta \ln \rho_{\mathrm{est}}$, as expected from the visualization of $\mathbf{R}$. The amplitude of contamination into $\delta \ln V_{S\,\mathrm{est}}$ is very small, and is well below the level of signal obtained in real data inversions, so it should not be a problem. The amplitude of contamination into $\delta \ln \rho_{\mathrm{est}}$ is also not very large, but patterns at certain depths, particularly at 2800 km, are reminiscent of patterns from recent density models inverted from normal-mode splitting coefficients (Ishii & Tromp 1999, 2001), where high-density features are located over Africa, and the Pacific basin region. In the upper mantle, there is significant contamination of $\delta \ln V_P$ patterns into $\delta \ln \rho$. In Fig. 4, $\delta \ln V_S$ is well resolved, with insignificant contamination into $\delta \ln V_{P\,\mathrm{est}}$. The contamination amplitude into $\delta \ln \rho_{\mathrm{est}}$ is somewhat higher, and the patterns mapped into the density model appear as high densities in areas of slab subduction in the circum-Pacific regions, especially at the bottom of the mantle. In the upper mantle, the same patterns of contamination in $\delta \ln \rho$ from $\delta \ln V_S$ appear as in Fig. 3, but at somewhat stronger amplitudes. Finally, in Fig. 5, we see that $\delta \ln \rho$ can be recovered in the absence of $\delta \ln V_S$ and $\delta \ln V_P$ structure, and there is not significant contamination into $\delta \ln V_{P\,\mathrm{est}}$ and $\delta \ln V_{S\,\mathrm{est}}$ in amplitude and pattern.

The results of an analogous experiment, not shown here, indicate that, for spatial parametrization $s_{\max} = 6$, $p_{\max} = 10$, the contamination effects are similar to the effects for spatial parametrization $s_{\max} = 6$, $p_{\max} = 7$.

Cumulative contamination

As seismic velocity structure in the Earth is relatively well documented (e.g. Su *et al.* 1994; Li & Romanowicz 1996; Masters *et al.* 1996; Dziewonski *et al.* 1997; Vasco & Johnson 1998; van der Hilst *et al.* 1997), the study of cumulative contamination of $\delta \ln V_P$ and $\delta \ln V_S$ into $\delta \ln \rho$ can be particularly informative. To investigate the latter, we have performed a series of tests (labelled C–J), in which we vary the depth parametrization ($p_{\max} = 7$ versus $p_{\max} = 10$) and the input $\delta \ln V_S$ model, keeping the input model in $\delta \ln \rho$ to be zero. Table 3 describes the details of each experiment.
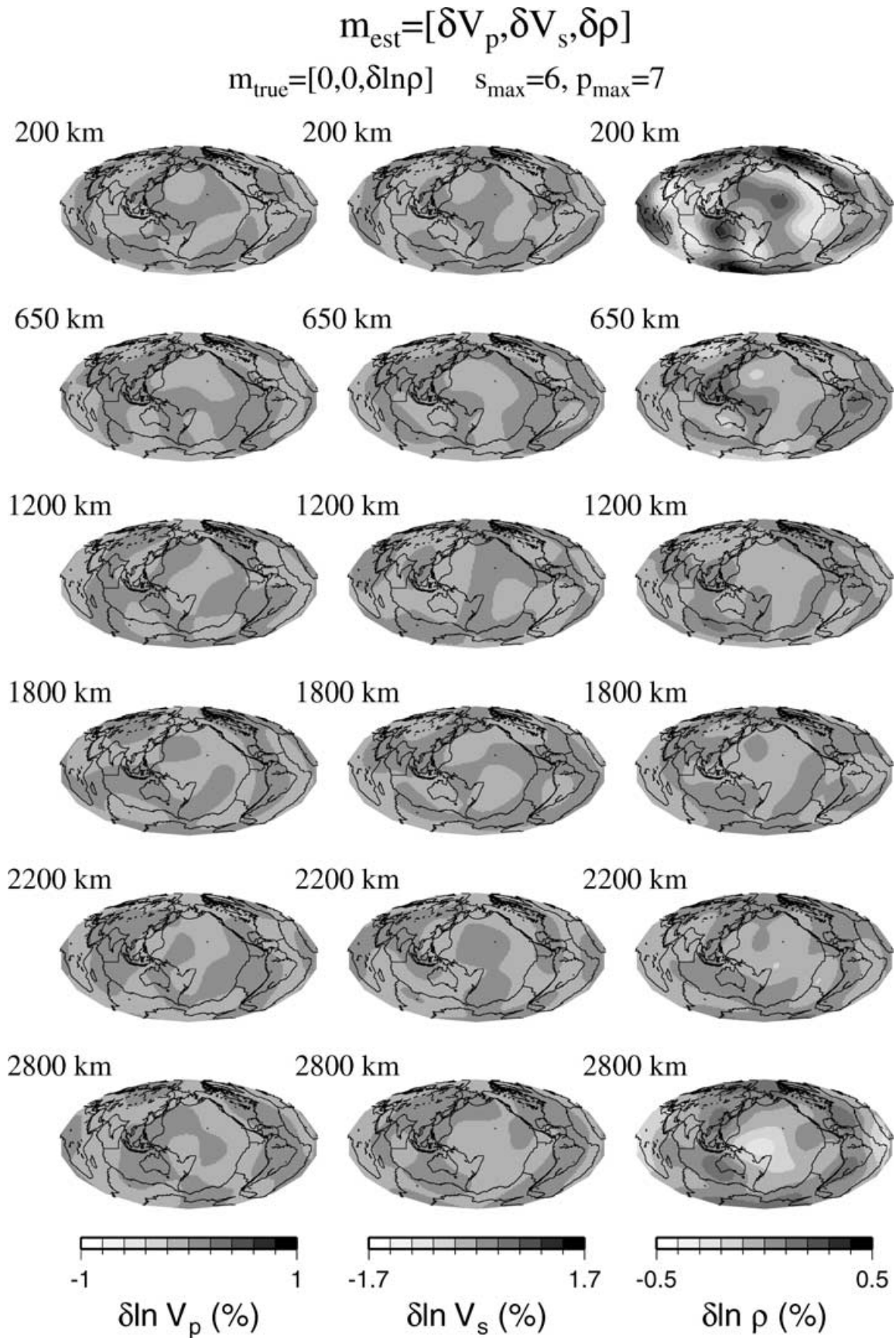
The comparison of the models obtained in experiments C and D (same initial models, different depth parametrization) with those of experiments A and B, respectively, indicates that the velocity structures are well recovered, but a spurious density structure is introduced in C and D. This density structure is well correlated with that obtained in A and B, where the starting model was a realistic density model (Figs 6b and d). The maps of 'ghost' density patterns for degrees two, four and six are shown in Figs 7(a) and (b) for experiments C and D. Only the even degrees are displayed to compare directly with published density models, even though the

$$m_{est}=[\delta V_p, \delta V_s, \delta\rho]$$

$$m_{true}=[\delta\ln V_p, 0, 0] \qquad s_{max}=6, p_{max}=7$$
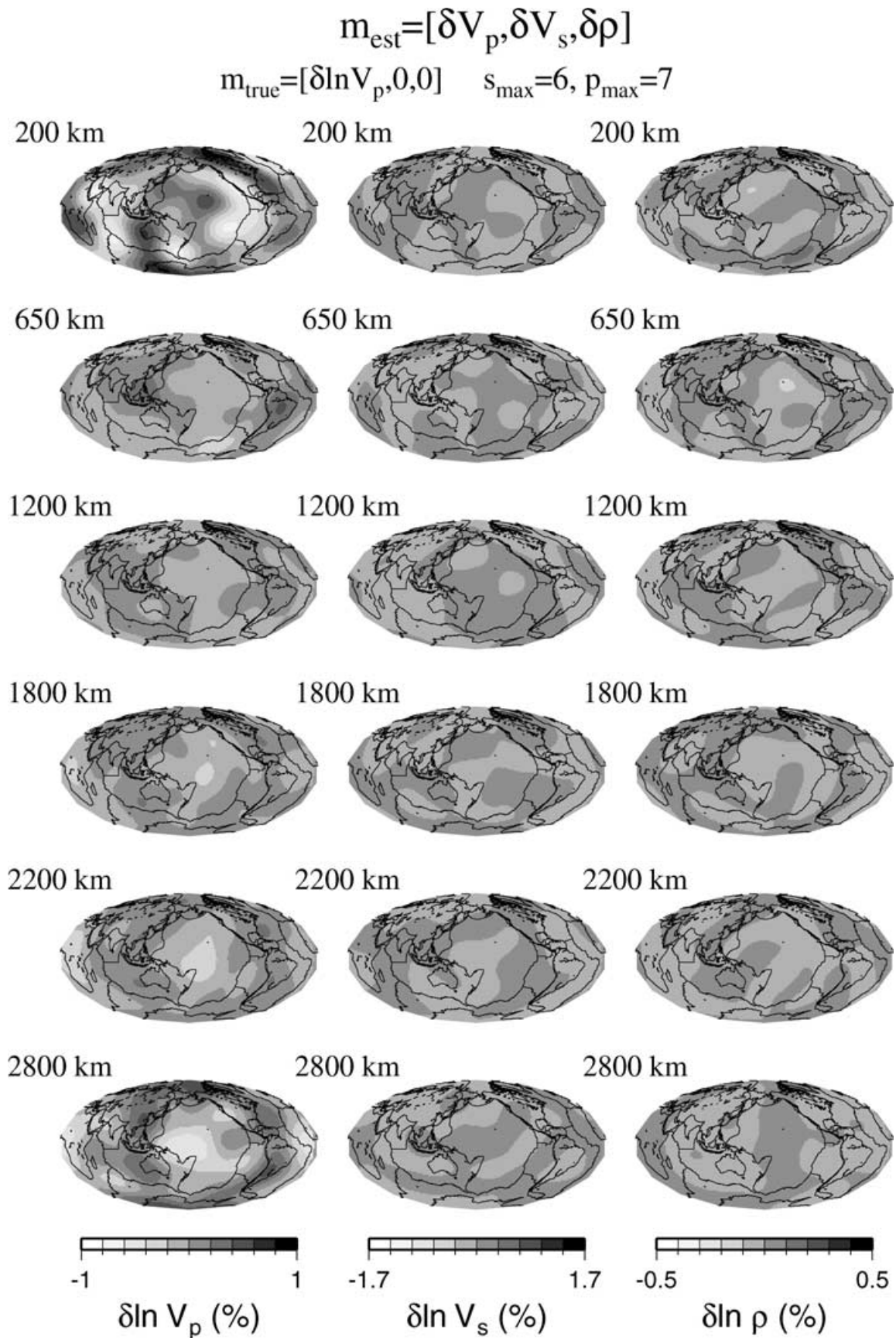
Figure 3. The output model of perturbations in V_p, left-hand column, V_s, middle column and ρ, right-hand column, for an input model $\mathbf{m}_{true} = [\delta \ln V_p, 0, 0]$, where $\delta \ln V_p$ is $0.5 \times$ SAW12D (Li & Romanowicz 1996). The spatial parametrization for the resolution matrix is $s_{max} = 6$, $p_{max} = 7$.

$$m_{est}=[\delta V_p, \delta V_s, \delta \rho]$$

$$m_{true}=[0, \delta \ln V_s, 0] \qquad s_{max}=6, \ p_{max}=7$$
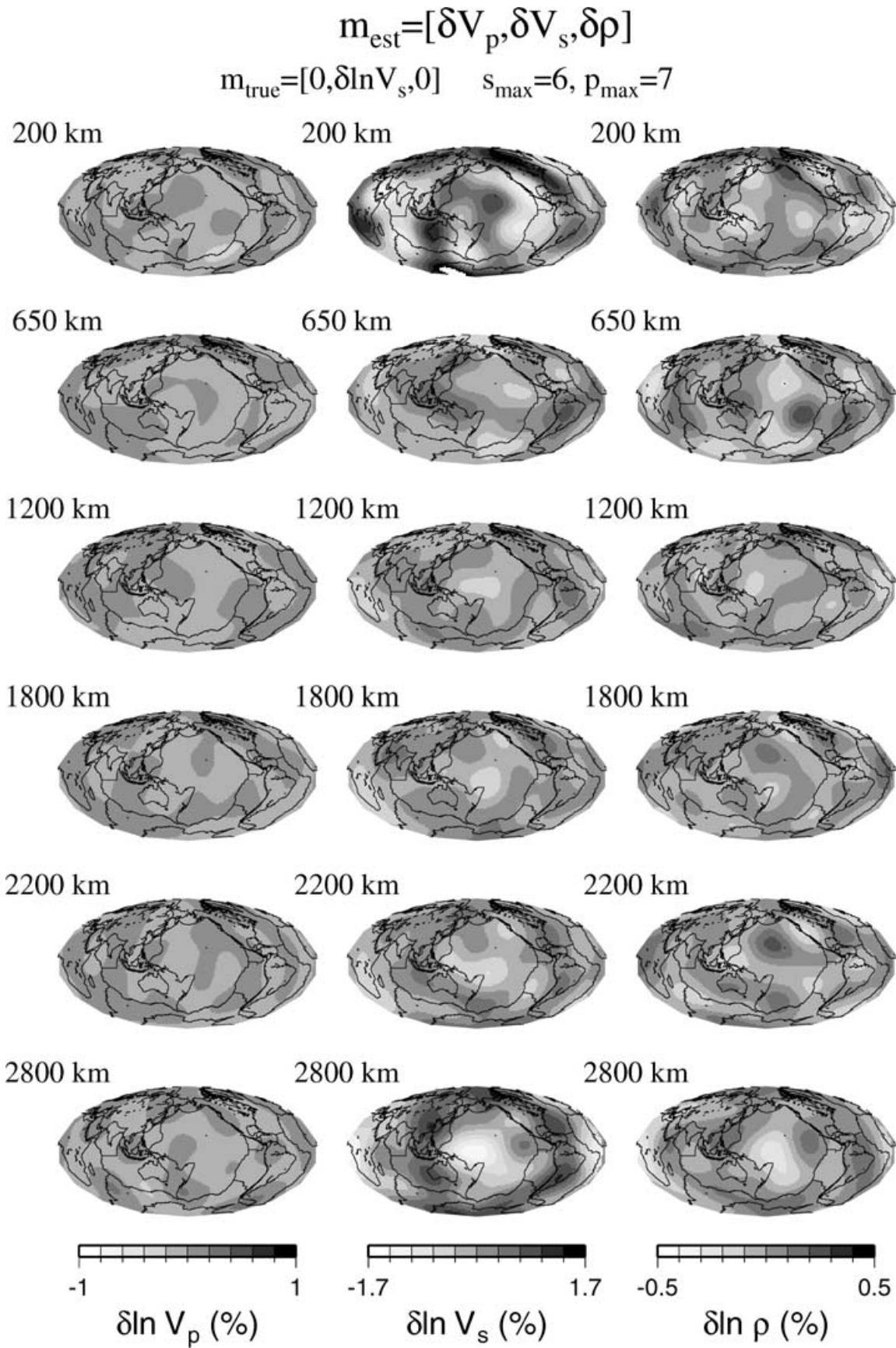
Figure 4. The output model of perturbations in V_p, left-hand column, V_s, middle column and ρ, right-hand column, for an input model $\mathbf{m}_{true} = [0, \delta \ln V_s, 0]$, where $\delta \ln V_s$ is SAW12D (Li & Romanowicz 1996). The spatial parametrization for the resolution matrix is $s_{max} = 6$, $p_{max} = 7$.

$$m_{est}=[\delta V_p,\delta V_s,\delta\rho]$$
$$m_{true}=[0,0,\delta\ln\rho] \qquad s_{max}=6,\ p_{max}=7$$

200 km   200 km   200 km

650 km   650 km   650 km

1200 km   1200 km   1200 km

1800 km   1800 km   1800 km

2200 km   2200 km   2200 km

2800 km   2800 km   2800 km

-1   1   -1.7   1.7   -0.5   0.5

$\delta\ln V_p$ (%) $\delta\ln V_s$ (%) $\delta\ln\rho$ (%)

Figure 5. The output model of perturbations in V_p, left-hand column, V_s, middle column and ρ, right-hand column, for an input model $\mathbf{m}_{true} = [0, 0, \delta\ln\rho]$, where $\delta\ln\rho$ is $0.25 \times$ SAW12D (Li & Romanowicz 1996). The spatial parametrization for the resolution matrix is $s_{max} = 6$, $p_{max} = 7$.

Table 3. Experiments of input $\mathbf{m}_{\text{true}} = [\delta V_p, \delta V_s, \delta\rho]$ are tabulated. For all experiments, the same norm damping is used for $\delta V_p, \delta V_s, \delta\rho$ in the determination of m_{est}.

Experiment	Spatial parametrization		δV_p^{true} model P16B30[1]	δV_s^{true} model		$\delta\rho^{\text{true}}$ model		
	$s = 6$ $p = 7$	$s = 6$ $p = 10$		SAW12D[2]	SH12WM13[3]	0	R25	R50
Resolution matrix tests								
A	★		★	★			★	
B		★	★	★			★	
C	★		★	★		★		
D		★	★	★		★		
E	★		★		★	★		
F		★	★		★	★		
H	★		★	★				★
I		★	★	★				★
Inversions w/synthetic seismograms								
J	★		★		★	★		
K		★	★		★	★		

The δV_p and δV_s models are from [1]Bolton (1996), [2]Li & Romanowicz (1996) and [3]Su *et al.* (1994).

odd-degree model parameters are not very large and do not have much of an impact on the displayed images. High-density regions corresponding to regions of slab subduction exist at many depths. In fact, the patterns of $\delta \ln \rho_{\text{est}}^C$ and $\delta \ln \rho_{\text{est}}^D$ are similar to density models obtained from inversions of spectral data, which we call R_NMSPEC (Fig. 7c) (Kuo *et al.* 1998; Kuo & Romanowicz 1999a,b). The model R_NMSPEC is spatially parametrized to $s_{\text{max}} = 6$ and $p_{\text{max}} = 7$, and no *a priori* assumptions are imposed for the inversion of observed spectral data. The correspondence between Figs 7(a) and (c) shows that if P16B30 and SAW12D are representative of the seismic velocity perturbations in the real Earth, the artefact density models puts into question the confidence we have in the density models obtained from the inversions of the normal-mode spectra. Although the amplitudes of the artefact density models are much smaller than the density features in models derived from real data, the similarity in pattern cannot be ignored, given that the mantle density structure is not well established. We will show in a following section that artefact density amplitudes derived from complete non-linear inversions of synthetic data are commensurate with amplitudes obtained using the real data.

If we use SH12WM13 (Su *et al.* 1994), as a starting model for $\delta \ln V_S$ (experiments E and F), the ghost density model retrieved is somewhat different. In experiment F, the resulting ghost density model for a $s_{\text{max}} = 6$, $p_{\text{max}} = 10$ parametrization yields patterns that are strongly reminiscent of the published density model SPRD6 of Ishii & Tromp (1999), particularly the high-density feature in the Pacific basin and over Africa at 2800 km. From Figs 8(b) and (c), the density patterns from $\delta \ln \rho_{\text{est}}^F$ and SPRD6 (Ishii & Tromp 1999) can be directly compared for six depths in the mantle. The resemblance is striking, although the amplitudes of $\delta \ln \rho_{\text{est}}^F$ are much smaller in the lower mantle, and there are slight lateral shifts in the distribution of the patterns between $\delta \ln \rho_{\text{est}}^F$ and $\delta \ln \rho_{\text{est}}$ of SPRD6 (Ishii & Tromp 1999). There is less resemblance to the SPRD6 density model for the $p_{\text{max}} = 7$ parametrization in experiment E (Fig. 8a), but high-density ghost features also appear in the Pacific Basin at 2800 km.

In Fig. 9(a) and (b) we show the results of the same experiment, after iterating the process, using the resolution matrix, three times, to verify that the ghost features observed are not just a result of the use

of the linear approximation. For both parametrizations, the patterns remain stable after three iterations. For the $p_{\text{max}} = 7$ parametrization, the amplitudes are also stable. However, for the $p_{\text{max}} = 10$ parametrization, they increase after each iteration, reaching values that are commensurate with those of SPRD6. On the other hand, the associated velocity perturbation amplitudes remain stable. This shows, in particular, that, in this case, the overparametrization needs to be compensated by stronger damping. In any case, in order to be resolved, any real density signal would have to be stronger than the ghost signal that is being damped.

Comparing these results with the previous resolution matrix experiments C–F, it appears that the presence of the high-density feature in the central Pacific at the bottom of the mantle is sensitive to the starting *S* velocity model: when SH12WM13 is used, it is present (Fig. 8), but not when SAW12D is used as a starting model (Fig. 7).

While regularization schemes used in resolution tests are not directly applicable to the inversion of observed data (Resovsky & Ritzwoller 1999a) owing to the effects of noise, the damping scheme that we use is quite simplistic in $\mathbf{C}_m^{-1}$ and is imposed in the absence of noise. Despite this simplistic damping scheme, we can retrieve ghost density models that mimic density models inverted from data. Tests of model robustness by considering random noise in the data (Ishii & Tromp 1999) can still stably produce density models such as in Fig. 8(b), since the contamination in the density model parameter space is a result of coherent rather than random noise. Tests involving random noise to quantitatively understand its effects against this kind of coherent noise will be performed in the future. On the other hand, the dependence of the ghost density patterns on the V_s structure can be anticipated by inspection of the Backus–Gilbert kernels for the modes in this data set. These kernels show a sensitivity of density to uppermost and lowermost mantle V_s structure (Ishii & Tromp 1999, supplementary Fig. 6C), especially when one takes into account that the V_s heterogeneity is likely to be a factor of 3 or 4 larger than the ρ heterogeneity.

Of course, the contamination effect is more important for a low level of signal in $\delta \ln \rho_{\text{true}}$, and for larger levels of signal in $\delta \ln \rho$, it may still be possible to retrieve some information, especially by applying an appropriate damping scheme. However, the confidence
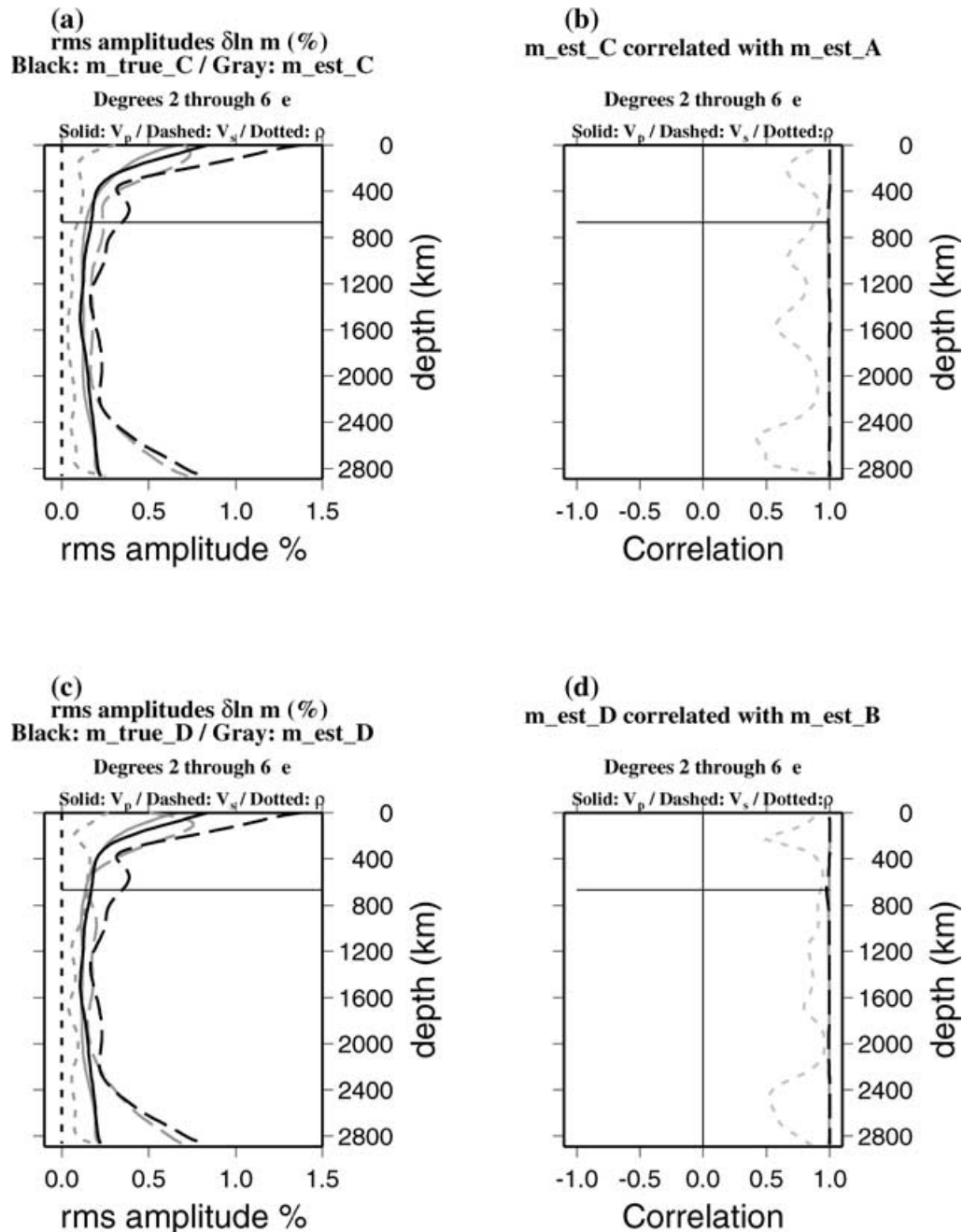
Figure 6. (a) For experiment C, the root-mean-squared amplitudes of an input model $\mathbf{m}_{\text{true}}$ in black lines, and output model $\mathbf{m}_{\text{est}}$ from a resolution matrix test, in grey lines. The dashed lines are $\delta \ln V_s$, the solid lines are $\delta \ln V_p$, and the dotted lines are $\delta \ln \rho$ rms amplitudes. See Table 1 for a description of input models. The input $\delta \ln \rho_{\text{true}} = 0$ (black dotted line). The retrieved $\delta \ln \rho_{\text{est}}$ (grey dotted line) has rms amplitudes >0. (b) Correlation of model $\mathbf{m}_{\text{est}}^{C}$ with model $\mathbf{m}_{\text{est}}^{A}$. (c) Same as (a) for experiment D. The retrieved $\delta \ln \rho_{\text{est}}$ has rms amplitudes >0. (d) Correlation of model $\mathbf{m}_{\text{est}}^{D}$ with model $\mathbf{m}_{\text{est}}^{B}$.

in the resulting model will always be marginal since we do not *a priori* know the level of density heterogeneity in the real Earth, in the absence of sufficient mineral physics information. Confidence tests may require supplementation by independent information, such as constraints provided by fits to the observed geoid. Although Ishii & Tromp (1999) have used geoid data to constrain their density model, they acknowledged themselves that these constraints were weak. This is to be expected in the absence of a well-constrained viscosity profile in the mantle, since without such constraints, the viscosity profile can be adjusted so that the geoid can be fitted with a wide range of density models (Panasyuk *et al.* 1999).

Likewise, the experiments we have performed using the geoid to try to discriminate between models with negative and positive $\delta \ln \rho / \delta \ln V_s$ ratios at the base of the mantle have not been conclusive.

Tests with density input models of different amplitudes

Experiments A–F have demonstrated that density perturbation amplitudes that are about 25 per cent of $\delta \ln V_s$ cannot be retrieved with confidence. The estimated models of density in experiments A and B, in which a mock input density model is used, are highly
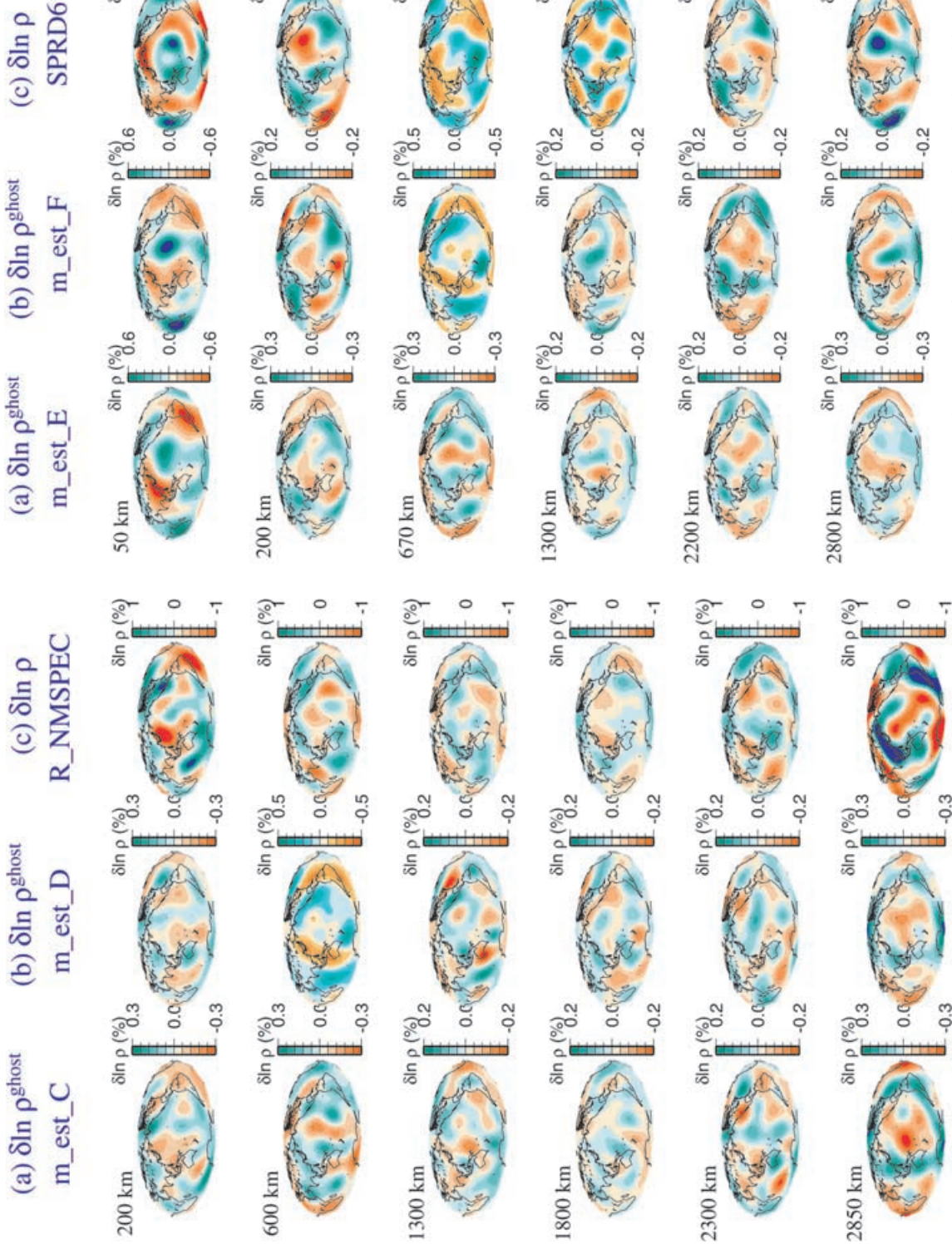
Figure 7. Even degrees two, four and six of retrieved model (a) $\delta \ln \rho_{est}^{C}$, (b) $\delta \ln \rho_{est}^{D}$ are shown for six depths in the mantle. We call $\delta \ln \rho_{est}^{C}$ and $\delta \ln \rho_{est}^{D}$ 'ghost' density models because the input model is m_{true} = [P16B30, SAW12D, 0] for s_{max} = 6, p_{max} = 7 and s_{max} = 6, p_{max} = 10, respectively. (c) The even degrees two, four and six of a density model (Kuo & Romanowicz 1998, 1999) retrieved from normal-mode spectra is shown for comparison with columns (a) and (b).

Figure 8. Even degrees two, four and six of retrieved model (a) $\delta \ln \rho_{est}^{E}$, (b) $\delta \ln \rho_{est}^{F}$ are shown for six depths in the mantle. We name $\delta \ln \rho_{est}^{E}$ and $\delta \ln \rho_{est}^{F}$ 'ghost' density models because the input model is m_{true} = [P16B30, SH12WM13, 0] for s_{max} = 6, p_{max} = 7 and s_{max} = 6, p_{max} = 10, respectively. (c) The even degrees two, four and six of the density model of SPRD6 (Ishii & Tromp 1999), at six mantle depths, is shown for comparison with columns (a) and (b). SPRD6 is inverted from normal-mode splitting coefficients.
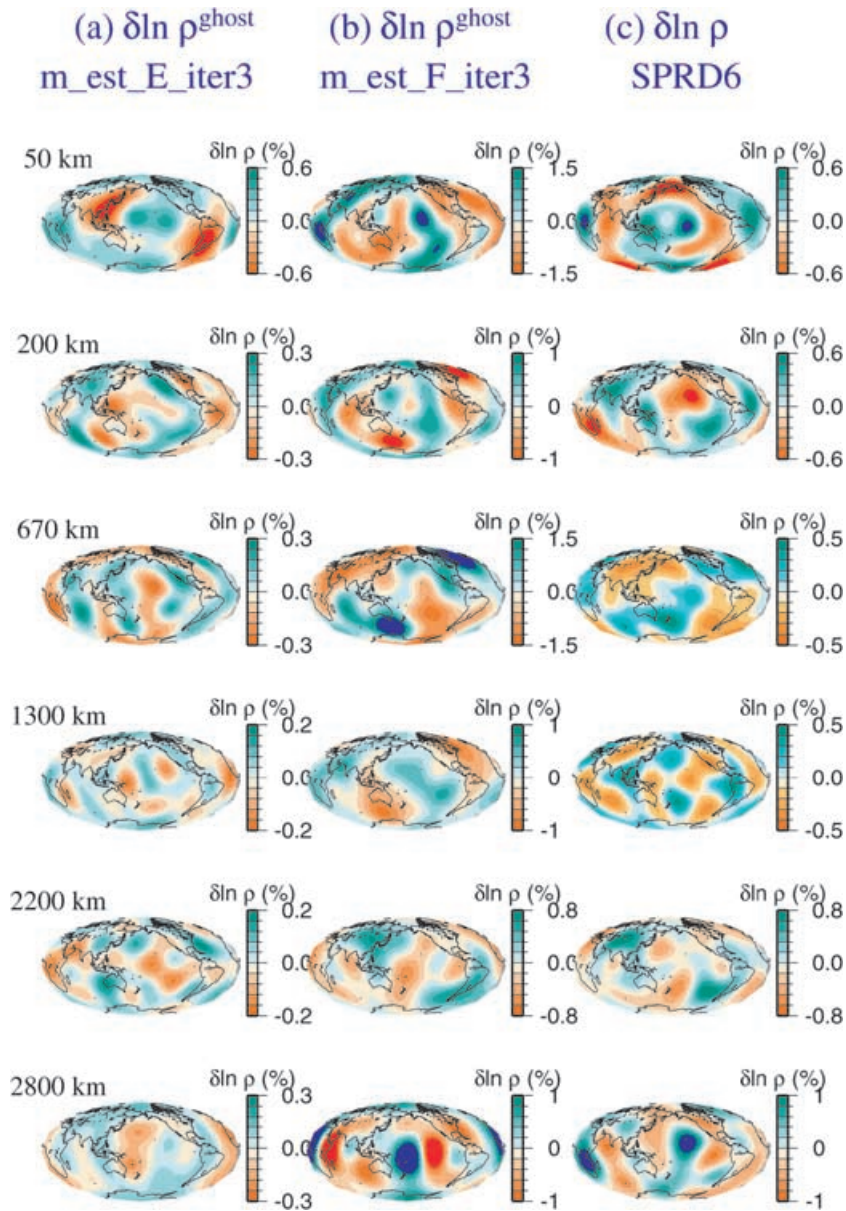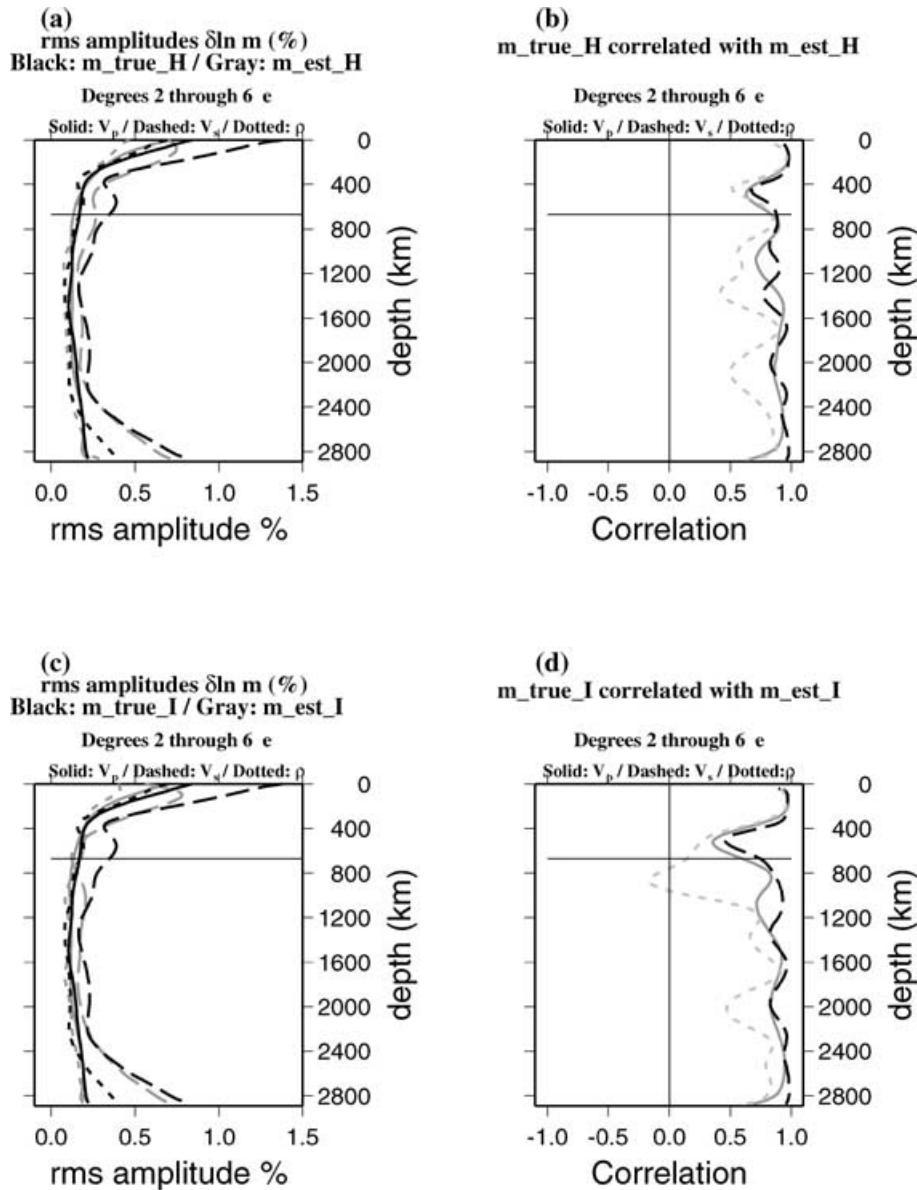
Figure 9. (a) and (b) The same as for Fig. 8(a) and (b) after iterating 3 times using the resolution matrix. (c) The same as Fig. 8(c). Note from the colour bars that the amplitudes between Figs 8(a) and 9(a) are more or less the same, while the amplitudes of the iterated $\delta \ln \rho_{est}^{F}$ in 9(b) is increased with respect to those in Fig. 8(b).

correlated with the estimated densities of experiments C and D, for which no input density was used. The high correlation demonstrates that contamination from seismic velocity signal swamps out the density signal in experiments A and B. The level of density perturbation signal in the Earth that can be detected needs to be investigated. To do so we refer to experiments A, B and H, I (Table 3) in which we, respectively, consider two input density models that differ only by an amplitude scaling factor. The mock density perturbations in model R50 have twice the amplitudes of those in model R25.

Figs 10(a) and (c) show the initial and recovered rms amplitudes as a function of depth. We note that, for both depth parametrizations, the level of density heterogeneity is poorly recovered in the last 400 km of the mantle. On the other hand, at the level of density signal in R50, Fig. 10(b) shows that the input $\delta \ln \rho_{true}^{H}$ is corre-

lated with the output $\delta \ln \rho_{est}^{H}$ much better than when the density signal is that of R25 (Fig. 1b), indicating that density can be resolved better for R50 than for R25. Overall, this is true for the correlation of $\delta \ln \rho_{true}^{I}$ and $\delta \ln \rho_{est}^{I}$ in comparison with the correlation of $\delta \ln \rho_{true}^{B}$ and $\delta \ln \rho_{est}^{B}$ (Figs 10d and 1d), but for this radial parametrization, $p_{max} = 10$, the density correlation in experiment I is poor below the transition zone down to 1200 km depth. This indicates that experiment I is overparametrized, leading to deficiencies in resolution.

Next, we correlate the $\delta \ln \rho_{est}$ in experiments H and I with ghost density estimates from experiments C and D. Correlation of $\delta \ln \rho_{est}^{H}$ with the ghost density model $\delta \ln \rho_{est}^{C}$ is decreased in comparison with Fig. 6(b), as shown in Fig. 11(a). However, $\delta \ln \rho_{est}^{I}$ correlates above 50 per cent with the ghost density model $\delta \rho_{est}^{D}$ in over three-quarters of the mantle, shown in Fig. 11(b).

(a)
**rms amplitudes δln m (%)**
Black: m_true_H / Gray: m_est_H

Degrees 2 through 6 e

Solid: V$_p$ / Dashed: V$_s$ / Dotted: ρ

(b)
m_true_H correlated with m_est_H

Degrees 2 through 6 e

Solid: V$_p$ / Dashed: V$_s$ / Dotted: ρ

(c)
rms amplitudes δln m (%)
Black: m_true_I / Gray: m_est_I

Degrees 2 through 6 e

Solid: V$_p$ / Dashed: V$_s$ / Dotted: ρ

(d)
m_true_I correlated with m_est_I

Degrees 2 through 6 e

Solid: V$_p$ / Dashed: V$_s$ / Dotted: ρ

Figure 10. For experiments H and I, the same as in Fig. 1.

These tests demonstrate that for the 44 spheroidal modes that we use in our data set, the radial parametrization $p_{max} = 7$ can begin to retrieve density patterns over the contamination signal if the amplitudes of density perturbations are 50 per cent of the V_s perturbation amplitudes, that is, a little less than 2 per cent for $\delta\rho/\rho$ in the shallow mantle. In addition, models parametrized to higher orders, such as $p_{max} = 10$, suffer in resolving power if not sufficiently damped or smoothed. For this to be the actual situation in the Earth, real density fluctuations would need to differ by as much as a factor of 2 compared with the results of laboratory measurements (e.g. Karato 1993).

Although the density models obtained from normal-mode data (Ishii & Tromp 1999, 2001; Kuo 1999; Kuo & Romanowicz 1999a,b) currently resemble the ghost density patterns from experiments C–F, the Earth's 3-D density structure could still be resolved, if the perturbations are large enough. However, the expected amplitude of density perturbations owing to slabs at high pressures and temperatures (Panero 2001) is 1–2 per cent. If the localized inclusions suggested by the high-pressure and high-temperature experiments are pervasive in the mantle, then they may constitute large-scale structure to which the modes may be sensitive. Then, the density signal may be at the limit of being resolvable, so that even if there is a real signal in the density models derived from data, it may very probably be overwhelmed by contamination. The plots in Figs 6(a) and (c) show that the contaminant density amplitudes can be commensurate with the amplitudes in R50 (left-hand plot in Fig. 10a). Inversions with real data can yield density amplitudes greater than those in R50, but before assuming that the amplitudes are an indication of large signal, one must ensure that the amplitudes are not a result of coherent errors from contamination producing such an amplified signal. It is not clear that applying stronger damping to reduce the effect of the coupling between physical model parameters in the resolution matrix will help bring out the real density signal.
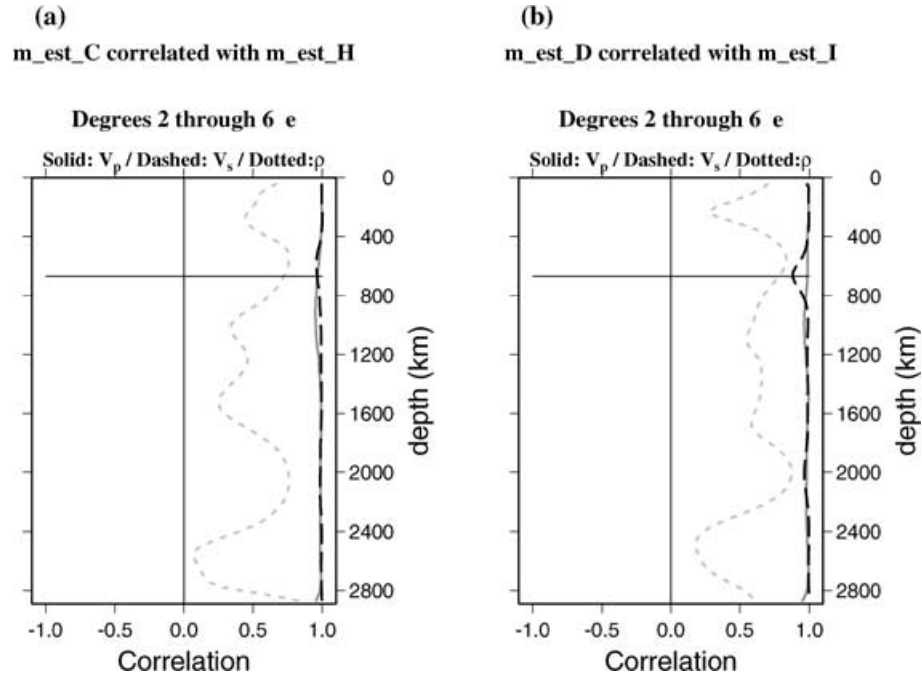
Figure 11. Correlations of estimated models for which input density is zero (experiments C and D) with estimated models for which input density is a mock model R50 (experiments H and I). (a) Correlation between $\mathbf{m}_{\mathrm{est}}^{C}$ and $\mathbf{m}_{\mathrm{est}}^{H}$, $s_{\max} = 6$, $p_{\max} = 7$, and (b) correlation between $\mathbf{m}_{\mathrm{est}}^{D}$ and $\mathbf{m}_{\mathrm{est}}^{I}$, $s_{\max} = 6$, $p_{\max} = 10$.

TESTS WITH SYNTHETIC SEISMOGRAMS

So far, we have only considered simple tests, to illustrate the sensitivity of the retrieved density models to assumptions on initial models and model parametrization, resulting from the structure of the resolution matrix. However, our particular inversion scheme is non-linear, and therefore involves several iterations, the results of which may not be completely represented by the resolution matrix corresponding to the first iteration only, if the non-linearity is too strong (e.g. Tarantola 1987). In what follows, we present more complete tests involving the computation of full synthetic seismograms and their iterative inversion, more accurately simulating the inversion process corresponding to real spectral data, as were performed in Kuo (1999), and as described in the introduction.

Specifically, we are interested in the contaminant signal in density resulting from our iterative inversion scheme. The spatial parametrization and input models of experiments E and F are revisited in experiments J and K (radial parametrization $p_{\max} = 6$ and 10, respectively, Table 3) whereby the estimated models $\mathbf{m}_{\mathrm{est}}^{J}$ and $\mathbf{m}_{\mathrm{est}}^{K}$ are now obtained from inversions of synthetic seismograms computed from input models $\mathbf{m}_{\mathrm{true}}^{J} = \mathbf{m}_{\mathrm{true}}^{K}$. $\mathbf{m}_{\mathrm{true}}^{J}$ and $\mathbf{m}_{\mathrm{true}}^{K}$ are composed of models P16B30 for $\delta \ln V_p$ and SH12WM13 for $\delta \ln V_s$, and there are no density perturbations. Aspherical structure up to harmonic degree 12 and radial order 13 is included in the computation of synthetic seismograms. We start the inversions from PREM (Dziewonski & Anderson 1981), and damp the second radial derivative to ensure radial smoothness. This damping parameter, denoted by η_3 (Li & Romanowicz 1996), for $\delta \ln V_p$ was required to be twice as strong as for either $\delta \ln V_s$ or $\delta \ln \rho$ to produce a radially smooth model. After four iterations, the models $\mathbf{m}_{\mathrm{est}}^{J}$ and $\mathbf{m}_{\mathrm{est}}^{K}$ converge to give 99.6 and 99.5 per cent fits to the synthetic data, respectively.

The two models $\mathbf{m}_{\mathrm{est}}^{J}$ and $\mathbf{m}_{\mathrm{est}}^{K}$ are extremely similar and we believe that this is a result of the choice of damping to smooth the radial models. At present, the radial damping η_3 applied for $\delta \ln V_p$ is insufficient and stronger damping should be applied. The root-mean-squared profile for $\delta \ln V_{P\,\mathrm{est}}$ shows a large bump in the lower mantle that corresponds to a decreased correlation between the input and output $\delta \ln V_p$ models at the same depths (Figs 12a–d).

The patterns of $\mathbf{m}_{\mathrm{est}}^{J}$ are shown in Fig. 14 for degrees one to six. The patterns of $\mathbf{m}_{\mathrm{est}}^{K}$ are so similar to $\mathbf{m}_{\mathrm{est}}^{J}$ that we omit their plots. The input model for $\mathbf{m}_{\mathrm{true}}^{J} = \mathbf{m}_{\mathrm{true}}^{K}$ is shown in Fig. 13 for comparison. Assessment of our inversion for density with real data, can be made by comparing $\mathbf{m}_{\mathrm{est}}^{J}$ with $\mathbf{m}_{\mathrm{true}}^{J}$. In particular, we can compare the density model obtained from normal-mode data (Figs 7c and 8c), with the ghost density patterns in the third column in Fig. 14. Many of the high-density features from our density models are also present, both in pattern and amplitude, in the ghost density model. Some of them, of course, could be real, such as high densities beneath the Americas and Asia at most depths in the mantle, where we expect high densities to correlate with high velocities in subduction zones. On the other hand, at the bottom of the mantle, where we cannot rely on our *a priori* intuitions, the density model inverted from normal-mode spectra does not have high-density structure in the Pacific and under Africa at 2800 km as do $\delta \rho_{\mathrm{est}}^{J}$ or $\delta \rho_{\mathrm{est}}^{K}$. However, these high-density features are present in the density model of SPRD6 (Ishii & Tromp 1999) at this depth.

DISCUSSION AND CONCLUSIONS

Current methods of retrieving 3-D mantle density structure from normal-mode spectra (Kuo & Romanowicz 1999b) and normal-mode splitting coefficients (Ishii & Tromp 1999) do not appear to yield reliable density models. Even though our mode data set is not
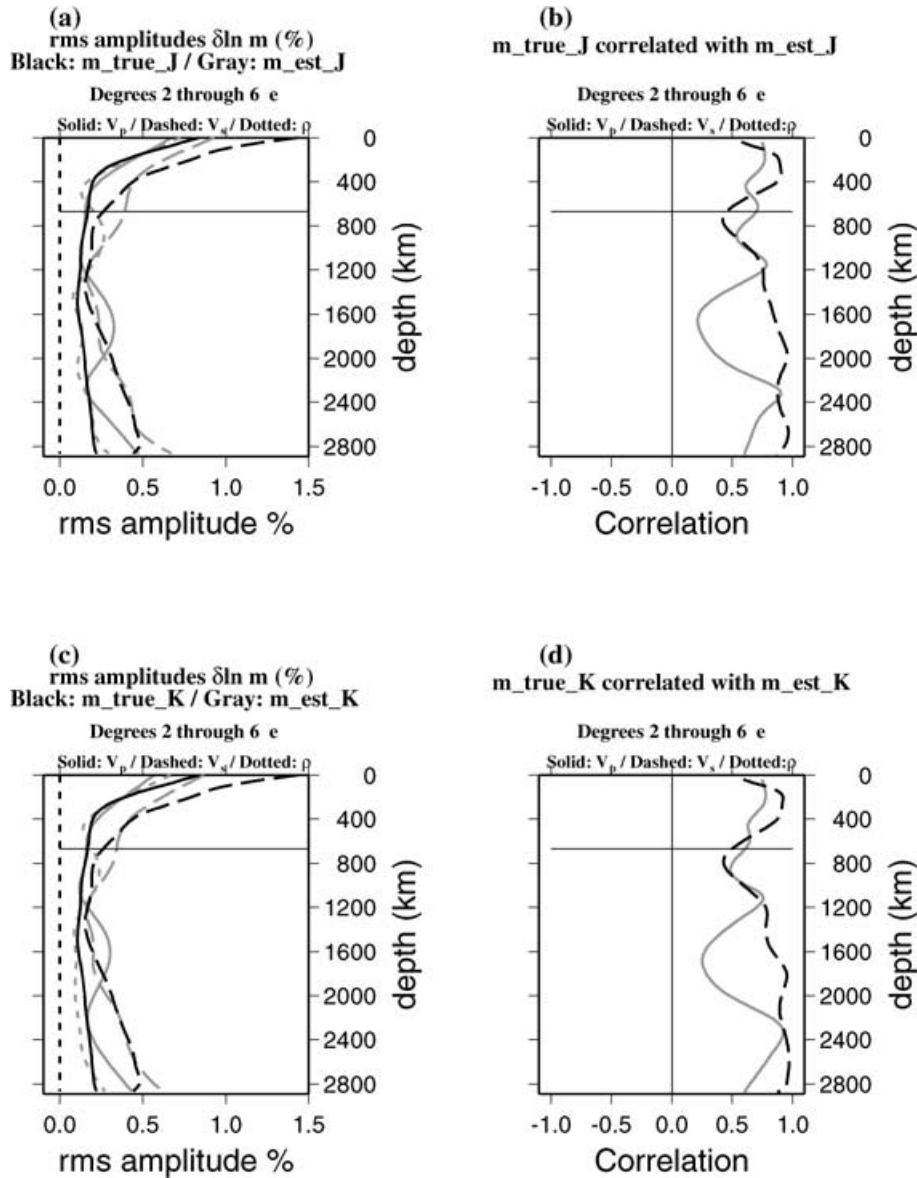
Figure 12. For experiments J and K, the same as in Fig. 1. There are no curves displaying correlation between $\delta\rho_{true}$ and $\delta\rho_{est}$ in plots (b) and (d) because the model for $\delta\rho_{true}$ is zero everywhere in experiments J and K, as shown in plots (a) and (c) as black dotted lines.

as large as that considered by the latter, in a different set of experiments, Romanowicz (2001) obtained equally good fits to degree-two splitting data for models with positive or negative $\delta \ln \rho / \delta \ln V_s$ ratios in the lowermost mantle, based on a comparable mode data set to that used by Ishii & Tromp (1999). The mantle density models are affected by the contamination of $\delta \ln V_P$ and $\delta \ln V_S$ structure into the density model space, and depend strongly on the *a priori* starting models in velocity, towards which the inversion is damped, at least for certain choices of depth parametrization.

Resovsky & Ritzwoller (1999a) have documented the instability of ρ models derived from normal-mode splitting coefficients when using a sweep of *a priori* constraints. They have shown that it is not possible to determine correlation and/or decorrelation of $\delta \ln \rho$ with seismic velocity perturbations as a function of depth. Our work supports their conclusions that current methods and data sets are not sufficient to uniquely determine the density structure of the Earth. We have shown that it is possible to retrieve models of

ρ perturbations purely as a result of contamination from V_S and V_P structure, and that these ghost ρ models are consistent in pattern and amplitude with published ρ models inverted from splitting coefficients (Ishii & Tromp 1999), or with ρ models that we determine from normal-mode spectral data (Kuo 1999), depending on the details of the test performed, and, in particular, the starting *S*-velocity model.

We have found that resolution tests involving linear products of resolution matrices with input Earth models devoid of density perturbations ($\mathbf{m}_{true} = [\delta \ln V_p, \delta \ln V_s, 0]$) produce ghost density models that closely resemble the density structure of SPRD6. Iterations on the models using the resolution matrix causes amplification of the ghost density model amplitude, but not of velocity structure amplitudes. To further investigate the effects of the non-linearity, we performed non-linear inversions of synthetic spectra, computed from the same input model $\mathbf{m}_{true} = [\delta \ln V_p, \delta \ln V_s, 0]$, and these tests produce a ghost density pattern that resembles density models
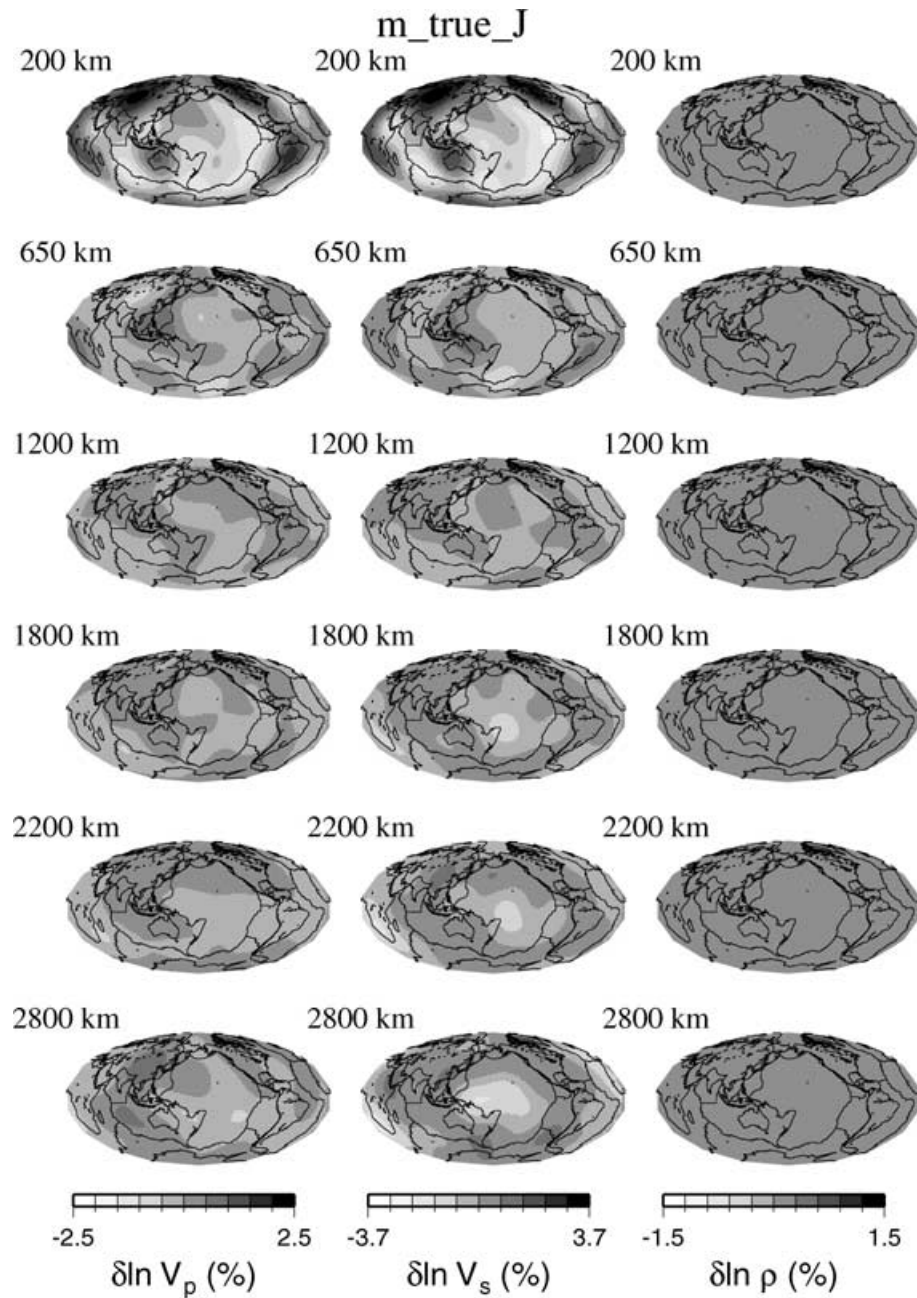
m_true_J

Figure 13. For experiments J and K (also E and F), the input model $\mathbf{m}_{\text{true}} = [\delta \ln V_p, \delta \ln V_s, 0]$ where $\delta \ln V_p = $ P16B30 (Bolton 1996), and $\delta \ln V_s = $ SH12WM13 (Su *et al.* 1994). As there are no density perturbations in $\mathbf{m}_{\text{true}}$, the input aspherical density model is zero everywhere.

estimated from normal-mode spectral data (Kuo & Romanowicz 1999a,b).

It may not be possible in the near future to resolve lateral density variations over the whole mantle independently of those of seismic velocities. However, at least in the upper mantle and down to the mid-mantle, reasonable assumptions concerning positive correlation between densities and seismic velocities can be made on the basis of: (1) mineral physics data and (2) geoid fits obtained using seismic velocity models converted into density. Also, Romanowicz (2001) showed that the scaling parameter $\delta \ln \rho / \delta \ln V_s$ can be constrained, at least for degree two, at the top of the mantle and down to about 1500 km depth. When a larger collection of upper and mid-mantle higher-frequency mode measure-

ments is included, as may be possible with the development of new data processing techniques (e.g. Widmer-Schnidrig 2002), this ratio may eventually be better constrained, at least in the top half of the mantle, and also at shorter wavelengths (e.g. Resovsky 2000).

ACKNOWLEDGMENTS
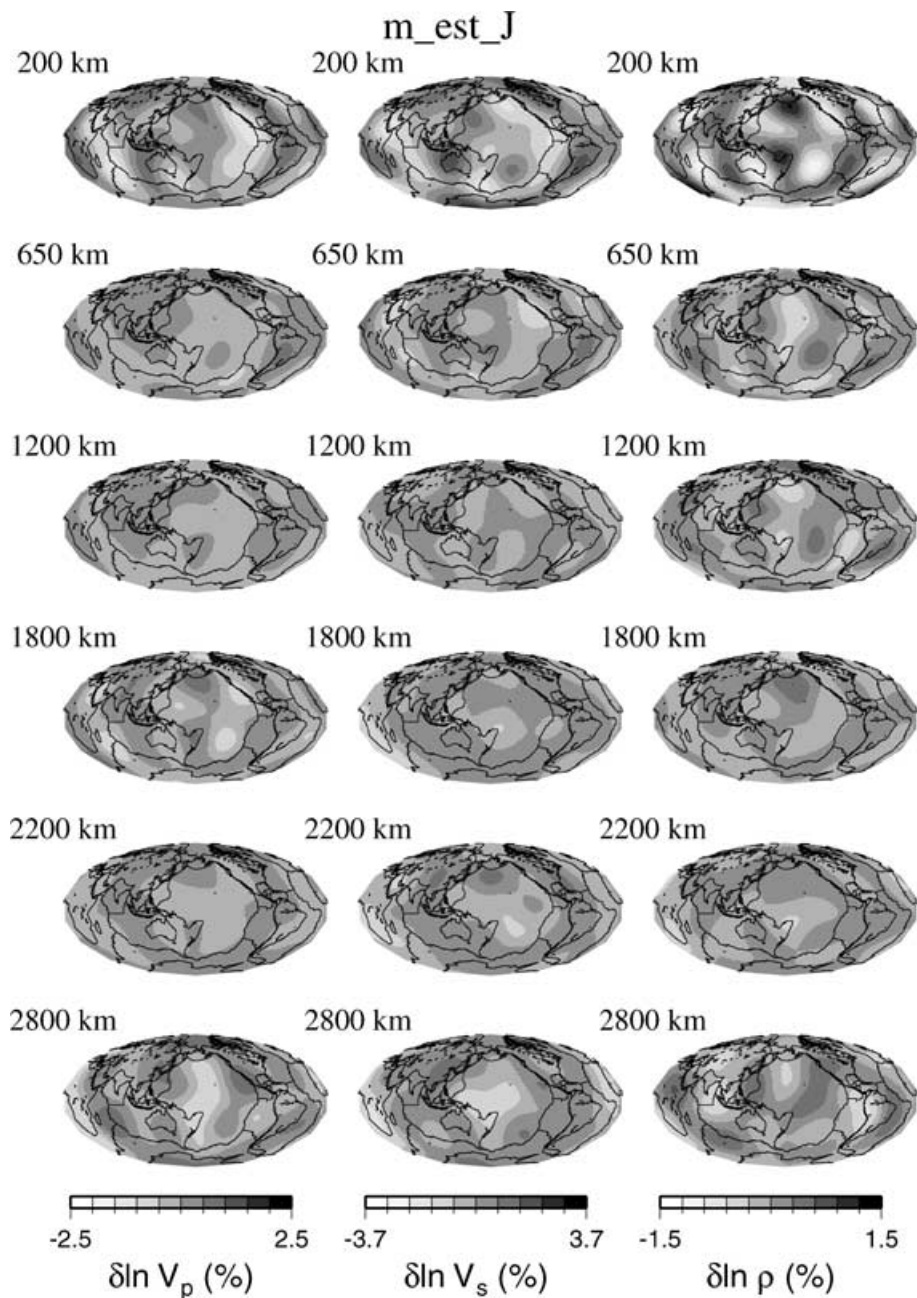
Figure 14. From resolution tests inverting synthetic seismograms, the output model of perturbations in V_p, left-hand column, V_s, middle column and ρ, right-hand column, for an input model $\mathbf{m}^J_{\text{true}}$. The spatial parametrization for this estimated model is $s_{\max} = 6$, $p_{\max} = 7$, whereas $s_{\max} = 12$, $p_{\max} = 13$ for the input model were used in the synthetic seismogram computations.

REFERENCES

Bolton, H., 1996. Long period travel times and the structure of the mantle, *PhD thesis,* University of California, San Diego, CA.

Dahlen, F.A., 1982. The effect of data windows on the estimation of free oscillation parameters, *Geophys. J. R. astr. Soc.,* **69,** 537–549.

Durek, J.J. & Romanowicz, B., 1999. Inner Core anisotropy inferred by direct inversion of normal mode spectra, *Geophys. J. Int.,* **139,** 599–622.

Dziewonski, A.M. & Anderson, D.L., 1981. Preliminary reference Earth model, *Phys. Earth planet. Inter.,* **25,** 297–356.

Dziewonski, A.M., Ekstrom, G. & Salganik, M.P., 1995. Centroid-moment tensor solutions for April–June 1994, *Phys. Earth planet. Inter.,* **88,** 69–78.

Dziewonski, A.M., Liu, X.-F. & Su, W.-J., 1997. In *Earth's Deep Interior:* the Doornbos Memorial Volume, pp. 11–50, ed. Crossley, D.J., Gordon and Breach Science, Newark, NJ.

Giardini, D., Li, X.-D. & Woodhouse, J.H., 1988. Splitting functions of long-period normal modes of the Earth, *J. geophys. Res.,* **93,** 13 716–13 742.

Giardini, D., Li, X.-D. & Woodhouse, J.H., 1987. Three-dimensional structure of the Earth from splitting in free-oscillation spectra, *Nature,* **325,** 405–411.

Ishii, M. & Tromp, J., 1998. Three-dimensional modeling of mantle heterogeneity and their implications for petrology, *EOS, Trans. Am. geophys. Un.,* **79,** F656.

Ishii, M. & Tromp, J., 1999. Normal-mode and free-air gravity constraints on lateral variations in velocity and density of Earth's mantle, *Science,* **285,** 1231–1236.

Ishii, M. & Tromp, J., 2001. Even-degree lateral variations in the Earth's mantle constrained by free oscillations and the free-air gravity anomaly, *Geophys. J. Int.,* **145,** 77–96.

Karato, S., 1993. Importance of anelasticity in the interpretation of seismic tomography, *Geophys. Res. Lett.,* **20,** 1623–1626.

Kuo, C., 1999. Three-dimensional density structure of the earth: limits of astrophysical and seismological approaches, *PhD thesis,* University of California, Berkeley, CA.

Kuo, C. & Romanowicz, B., 1999a. Three-dimensional density structure obtained by normal mode spectral measurements, *Proc., IUGG XXII General Assembly,* A62.

Kuo, C. & Romanowicz, B., 1999b. Density and seismic velocity variations determined from normal mode spectra, *EOS, Trans. Am. geophys. Un.,* **80,** S14.

Kuo, C., Durek, J. & Romanowicz, B., 1998. Mantle heterogeneity inferred from normal mode spectra, *EOS, Trans. Am. geophys. Un.,* **79,** F627.

Lévêque, J.J., Rivera, L. & Wittlinger, G., 1993. On the use of the checkerboard test to assess the resolution of tomographic inversions, *Geophys. J. Int.*, **115,** 313–318.

Li, X.-D. & Romanowicz, B., 1996. Global mantle shear velocity model developed using nonlinear asymptotic coupling theory, *J. geophys. Res.,* **101,** 22 245–22 272.

Li, X.-D., Giardini, D. & Woodhouse, J.H., 1991. The relative amplitudes of mantle heterogeneity in *P* velocity, *S* velocity and density from free-oscillation data, *Geophys. J. Int.,* **105,** 649–657.

Masters, G., Johnson, S., Laske, G. & Bolton, H., 1996. A shear-velocity model of the mantle, *Phil. Trans. R. Soc. Lond.,* A, **354,** 1385–1411.

Menke, W., 1989. *Geophysical Data Analysis: Discrete Inverse Theory,* revised edn, Academic, San Diego, CA.

Panero, W., 2001. Experimental observations of basaltic crust in the lower mantle, *PhD thesis,* University of California, Berkeley, CA.

Panasyuk, S., Ishii, M., O'Connell, R. & Tromp, J., 1999. Constraints on the density and viscosity structure of the earth, *EOS, Trans. Am. geophys. Un.,* **80,** F28.

Resovsky, J., 2000. Model space mapping quantifies uncertainty in 3-D density models, *EOS, Trans. Am. geophys. Un.,* **81,** F823.

Resovsky, J.S. & Ritzwoller, M.H., 1999a. Regularization uncertainty in density models estimated from normal mode data, *Geophys. Res. Lett.,* **26,** 2319–2322.

Resovsky, J.S. & Ritzwoller, M.H., 1999b. A degree 8 mantle shear velocity model from normal mode observations below 3 mHz. *J. geophys. Res.,* **104,** 993–1014.

Romanowicz, B., 2001. Can we resolve 3-D density heterogeneity in the lower mantle?, *Geophys. Res. Lett.,* **28,** 1107–1110.

Su, W.J., Woodward, R.L. & Dziewonski, A.M., 1994. Degree 12 model of shear velocity heterogeneity in the mantle, *J. geophys. Res.,* **99,** 6945–6980.

Tarantola, A., 1987. *Inverse Problem Theory: Methods for Data Fitting and Model Parameter Estimation,* New York, Elsevier.

van der Hilst, R.D., Widiyantoro, S. & Engdahl, E.R., 1997. Evidence for deep mantle circulation from global tomography, *Nature,* **386,** 578–584.

Vasco, D.W. & Johnson, L.R., 1998. Whole Earth structure estimated from seismic arrival times, *J. geophys. Res.,* **103,** 2633–2671.

Widmer-Schnidrig, R., 2002. Application of regionalized multiplet stripping to retrieval of aspherical structure constraints, *Geophys. J. Int.,* **148,** 201–214.

Woodhouse, J.H. & Dziewonski, A.M., 1984. Mapping the upper mantle: three-dimensional modeling of Earth structure by inversion of seismic waveforms, *J. geophys. Res.,* **89,** 5953–5986.

Woodhouse, J.H., Giardini, D. & Li, X.-D., 1986. Evidence for inner core anisotropy from splitting in free oscillation data, *Geophys. Res. Lett.,* **13,** 1549–1552.